remote sensing

MDPI

Article

Characteristics and Applications of the Ground-Based X Band Low Elevation Angle Brightness Temperatures under Low Sea State Based on Measured Data

Zhongqing Cao [1,2], Lixin Guo [1,*], Shifeng Kang [2], Xianhai Cheng [2], Qingliang Li [2], Leke Lin [2] and Yusheng Zhang [2]

1 School of Physics and Optoelectronic Engineering, Xidian University, No. 2, Taibai Road, Xi'an 710071, China; zqcao@xidian.edu.cn

2 National Key Laboratory of Electromagnetic Environment, China Research Institute of Radiowave, Propagation, Qingdao 266107, China; kangsf@crirp.ac.cn (S.K.); chengxh@crirp.ac.cn (X.C.); liql@crirp.ac.cn (Q.L.); linlk@crirp.ac.cn (L.L.); zhangys@crirp.ac.cn (Y.Z.)

* Correspondence: lxguo@xidian.edu.cn

Received: 20 April 2020; Accepted: 25 May 2020; Published: 28 May 2020

Abstract: In ground-based microwave radiometer remote sensing, low-elevation-angle (−3°~3°) radiation data are often discarded because they are considered to be of little value and are often difficult to model due to the complicated mechanism. Based on the observed X-band horizontal polarization low elevation angle microwave radiation data and the meteorological data at the same time, this study investigated the generation mechanism of low elevation angle brightness temperature (LEATB) and its relationship with meteorological data, i.e., temperature, humidity, and wind speed, under low sea state. As a result, one could find that the LEATB was sensitive to the atmosphere at the elevation angle between 1° to 3°, and a diurnal variation of the LEATB reached up to 10 K. This study also found a linear relationship between the LEATB and sea surface wind speed under low sea state at an elevation range from −3° to 0°, i.e., the brightness temperature decreased as the wind speed increased, which was inconsistent with the observations at the elevation angle from −10° to −5°. The variation of the LEATB difference according to the change in the over-the-horizon detection capability (OTHDC) of the shipborne microwave radar was examined to identify the reason for this phenomenon theoretically. The results showed that the LEATB difference was significantly influenced by a change in the OTHDC. Further, this study examined a remote sensing method to extract the sea surface wind speed data from experimental LEATB data under low sea state. The results demonstrated that the X-band horizontal polarization LEATBs were useful to retrieve the sea surface wind speed data at a reasonable accuracy—the root mean square error of 0.02408 m/s. Overall, this study proved the promising potential of the LEATB data for retrieving temperature profiles, humidity profiles, sea surface winds, and the OTHDC.

Keywords: low-elevation angle brightness temperature; ground-based microwave radiometer; remote sensing; sea surface wind speed; over-the-horizon detection capability

1. Introduction

Remote sensing of microwave radiation for atmosphere and ocean is an important and active research field and has produced many achievements that have been widely used [1,2]. Microwave radiometers can measure the ocean brightness temperature (TB) to within several tens of degrees Kelvin in relative accuracy. As multi-frequency dual-polarized TB observations at this accuracy contain significant information on the characteristics of the ocean surface wind speed, utilization of this information requires a knowledge of the relationship between TB and conventional oceanographic and meteorological parameters, which has been developed to maturity [3]. Sea surface radiation TBs at three fully polarimetric channels (10.7, 18.7, and 37.0 GHz) and vertically and horizontally polarized channels (6.8 and 23.8 GHz) have been used to monitor wind speeds over the sea surface by WindSat polarimetric radiometers [4]. Sea surface upwelling radiation TB data at 6.925, 10.65, and 18.7 GHz were used to measure wind speeds over the sea surface by advanced microwave scanning radiometer-E (AMSR-E), and the analysis resulted in the estimated bias and root mean square errors (RMSEs) of −0.126 and 1.191 m/s, −0.094 and 1.152 m/s, and −0.085 and 1.338 m/s, respectively [5]. Alternatively, sea surface radiation data at 36.5 GHz H- and V-pol from SAC-D (satélite de aplicaciones científicas-D)/aquarius microwave radiometer suggested an algorithm to estimate the sea surface wind speed [6]. At present, the researchers mainly pay attention to sea surface upwelling radiation under extreme weather conditions, such as high sea state and typhoon. Vertically and horizontally polarized sea surface upwelling brightness temperatures of WindSat at 6.8 and 10.7 GHz under conditions (the wind speed above 20 m/s) is applied to retrieve the sea surface wind speeds in Typhoon [7]. The wind speeds within super typhoon Nepartak have been retrieved using brightness temperatures at 6.9 and 10.7 GHz derived from the advanced microwave scanning radiometer 2 (AMSR2) sensor in the global change observation mission-water1 (GCOM-W1) satellite [8]. Based on the sea surface upwelling brightness temperatures, the soil moisture active passive (SMAP) L-band spaceborne radiometer has been used as a passive microwave sensor to retrieve the wind speed of tropical cyclones and severe storms [9,10].

Although ocean surface wind field can be measured by shore-based or shipborne high-frequency or X-band radars [11–13], ground-based microwave radiometers have been used to monitor the sea surface meteorological parameters. For example, Zhang et al. (2010) used a ground-based microwave radiometer to monitor sea surface parameters [14].

Ground-based microwave radiometers have been also often used to monitor the profiles of temperature, humidity, and pressure in the troposphere at real-time [15–17]. Several methods have been proposed to improve the resolution of height and distance in the inversion profile [18–20]. Further, ground-based microwave radiometers have been used for remote sensing of atmospheric refractivity and atmospheric duct in the literature [21,22]. To date, however, only high elevation angle TBs (>10°) have been actively applied, while low elevation angle brightness temperatures (LEATBs) are often discarded as they are regarded as impractical values by difficulty in modeling due to the complex formation mechanism. The elevation angle in this paper referred to the angle between the observation direction and the horizontal plane. When it is positive, the elevation angle and the zenith angle are complementary angles, that is, they add up to 90°.

As the K and V band microwaves located at the atmospheric absorption line are sensitive to the atmospheric temperature and humidity, the ground-based microwave radiation TBs of the K and V band are usually used in the remote sensing of an atmospheric profile, rather than the X band that is not sensitive to the atmospheric temperature and humidity when the elevation angle is higher than 10°. Ground-based microwave radiometers provide the multi-elevation-angle atmospheric radiation information through the elevation-angle-scanning measurement to improve the accuracy of the monitored atmospheric profile. At low elevation angles (LEAs) (−3°~3°), however, the radiation TBs of the K and V bands tend to be saturated, and the dynamic range decreases due to a longer path [21,23]. On the contrary, the sensitivity of the X band TBs to water vapor or temperature is greatly increased at LEAs. Especially, when the radiation transfers at LEAs, the weight of the lower troposphere in total TB becomes much larger, and more information on the lower troposphere is contained in the LEATBs. Therefore, extracting the LEATBs is essential to fully understand the mechanism of the lower troposphere.

The main objective of this study was to identify the physical mechanisms that are involved in the generation of the LEATBs and the relationship between the LEATBs and the environment profiles of the lower troposphere and sea surface parameters using the observation data of the X band horizontally polarized LEATB in September and October 2018 at the Yellow Sea near Qingdao area, China. We also investigated the potential usage of the LEATBs in the remote sensing of the sea surface wind speed. This paper is organized as follows, the data are presented in Section 2, and the analysis is described in Section 3. The potential applications are presented in Section 4. Conclusions are summarized in Section 5.

2. Data

To better understand the LEATB (elevation between −3° and 3°) over the sea, a LEATB measurement campaign in a maritime scenario was initiated by the China Research Institute of Radiowave Propagation (CRIRP) on the Yellow Sea near Qingdao area, China, in September and October 2018.

During the 2018 measurement campaign, the LEATB measurement was conducted by a ground-based horizontally polarized microwave radiometer operating at the frequency of 11 GHz with a bandwidth of 300 MHz. The TB measured by the ground-based microwave radiometer at a positive elevation angle is the atmospheric downwelling brightness temperature, and the TB measured at a negative elevation angle is the sea surface upwelling brightness temperature. The microwave radiometer system used in this measurement campaign was a full-power radiometer with a partially fed elliptic paraboloid antenna, whose equivalent aperture was 1.8 m. In the vicinity of 11 GHz, the antenna's 3 dB beam width was about 1.1°, and the servo's elevation angle pointing resolution was 0.01°. The antenna feed was fixed in the feed box and between the feed and the antenna surface was a radome made of wave-transparent material. The receiver was placed in a thermostatic box to maintain thermal stability, and the temperature stability of the feed box was better than 0.05k.

The spectral radiance (SR) of the observed scene B_{sc} in $\mathrm{Wm}^{-2}\mathrm{Hz}^{-1}sr^{-1}$ observed at the frequency f within the antenna beam of the radiometer was related to the output voltage U_{sc} of the radiometer via

$$U_{sc} = g(B_{sc} + B_R)^{\alpha} \tag{1}$$

where g is the gain, B_R is the receiver noise SR, and α is the nonlinearity parameter [24]. For convenience, when comparing measurements spectrally, it was common to express observed SR B_f in terms of Planck equivalent brightness temperatures T_B solving Planck's law

$$B_f = \frac{2hf^3}{c^2\left(e^{hf/kT} - 1\right)} \quad \mathrm{Wm}^{-2}\mathrm{Hz}^{-1}\mathrm{sr}^{-1} \tag{2}$$

where kT is the Boltzmann constant, h the Planck constant, and c the speed of light. If the observed scene was a blackbody, its T_B would be equal to its physical temperature. Thus, the SRs of calibrations loads could be directly obtained from Equation (2). The unknown parameters in Equation (1), i.e., g, B_R, and α could be determined using different calibration techniques. To obtain the three unknowns (g, B_R, α), three calibration points were necessary. The radiometer realized one point with its built-in ambient temperature blackbody. The second calibration point was a pyramidal foam absorber blackbody immersed in liquid nitrogen (LN2). The third reference was realized with a built-in noise diode, which was used to inject an additional signal into the radiometer's detector when viewing one of the other calibration targets. Hence, a new unknown, namely, the effective spectral radiance (SR) B_N of this noise source, was introduced. However, two additional calibration points closed the equation system by looking at both of the calibration targets with the noise source on. Equation (1) could be rewritten accordingly.

$$U_C = g(B_R + B_C)^{\alpha} \tag{3}$$

$$U_H = g(B_R + B_H)^{\alpha} \tag{4}$$

$$U_{CN} = g(B_R + B_C + B_N)^{\alpha} \tag{5}$$

$$U_{HN} = g(B_R + B_H + B_N)^{\alpha} \tag{6}$$

where the index C stands for cold (LN2), and the index H for hot (ambient target). The index N refers to the added noise signal. The equation system was solved numerically to obtain g, B_R, B_N, and α.

The built-in noise diodes were used as calibration standards once their equivalent SRs B_N were determined during a liquid nitrogen calibration. In the K band, the noise diode calibration could be used to update the system noise B_R and the gain g while observing the internal target with and without additional noise signal, assuming that the system's nonlinearity α could be constant for several months [25].

$$U_{H1} = g_1(B_{R1} + B_H)^{\alpha} \tag{7}$$

$$U_{HN1} = g_1(B_{R1} + B_H + B_N)^{\alpha} \tag{8}$$

where U_{H1}, U_{HN1} are the measured voltage by viewing the internal target with and without additional noise signal, respectively. B_{R1}, g_1 are the updated system noise B_R and gain, respectively. The radiation resolution of the microwave radiometer was <0.15K (1 s integral time). During the experiment, the diurnal drift of the radiometer measured TB was RMS < 1.4 K when estimating at a constant temperature blackbody. The microwave radiometer with an antenna at 8 m above sea level (ASL) was used to conduct observation experiments at point A, as shown in Figure 1 (The images in Figure 1 were provided by google earth). As shown in Figure 2, the microwave radiometer was used to measure the LEATB towards the open sea with a narrow beam width (approximately 1.1°). In order to reduce the sidelobe's influence of the radiometer antenna on the main lobe, a low sidelobe antenna was used to improve the main beam efficiency η_M [26].

$$\eta_M = \frac{\iint_{main\_beam} F_n(\theta,\varphi)d\Omega}{\iint_{4\pi} F_n(\theta,\varphi)d\Omega} \tag{9}$$

Figure 1. The location of the radiometer used in this study. Point A is located near Qingdao, Shandong province, China. The ground-based microwave radiometer was set up at point A for observation, facing the open ocean in the southwest direction. There are no islands within 300 km ahead in the observation direction of the radiometer. The images in this figure were provided by google earth.

In Equation (9), the integral range of the numerator is within the main beam, and the integral range of the denominator is the solid angle of 4π. $F_n(\theta,\varphi)$ is the antenna pattern, θ is the elevation angle, φ is the azimuth angle.

Figure 2. View of the X-band H-polarized microwave radiometer. The microwave radiometer with an antenna 8 m above sea level was mounted on a truck, and the automatic weather station about 30 m away from the microwave radiometer was fixed at 6 m above the sea level.

The scanning elevation angle measurement method was adopted by the radiometer to observe from −5° to 5° according to the preset sweep angle sequence. At each elevation angle, the antenna was fixed, and the radiometer conducted observation. When the observation of this elevation angle was completed, the antenna moved to the next elevation angle until all elevation angles were observed.

An automatic weather station (AWS) was located about 30 meters away from the radiometer to measure meteorological parameters, i.e., atmosphere temperature, humidity, pressure, wind speed, and wind direction at the surface (6 m ASL), as shown in Figure 2. A ground-based X-band VV polarized radar, located at point B in Figure 1, about 50 meters away from the radiometer at an altitude of 25 m ASL, was used to obtain the sea surface radar echo data in the same direction as the microwave radiometer. When the radar was in the working status, the microwave radiometer was kept in the non-working status to avoid microwave interference. The farthest distance of the sea surface echo data (R_{max}) was used to indicate the over-the-horizon detection capability (OTHDC) of the microwave radar at that moment. During the experiment, 22 September 2018, 23 September 2018, 12 October 2018, and 23 October 2018were the dates when the radar was turned on twice in a day while only once on 21 October 2018.

3. Analysis

Based on the observed X-band horizontal polarization low elevation angle microwave radiation data and the meteorological data, this chapter investigated the generation mechanism of X-band horizontal polarization LEATB and its relationship with meteorological data under low sea state. During the experiment in the Qingdao area in 2018, the LEATB and the meteorological parameters, such as temperature, humidity, and pressure, at the same time were measured, and the maximum sea surface echo range of microwave over-the-horizon radar was collected. The typical data measured during the experiment are shown in Figure 3. The TB data measured by the ground-based microwave radiometer are shown in Figure 3a,c,e,g. When the elevation angle was positive, the main TB component was the atmospheric downwelling radiation TB. When the elevation angle was negative, the main TB component was the upwelling radiation TB from the sea surface. The corresponding meteorological data obtained using the AWS are shown in Figure 3b,d,f,h. The LEATB data obtained were all under low sea state during the experiment period. Therefore, the data-based analysis in this paper was only applicable to the low sea state. Although some theoretical analysis and prediction had been made under high sea state, it still needs further support of measured data under high sea state.

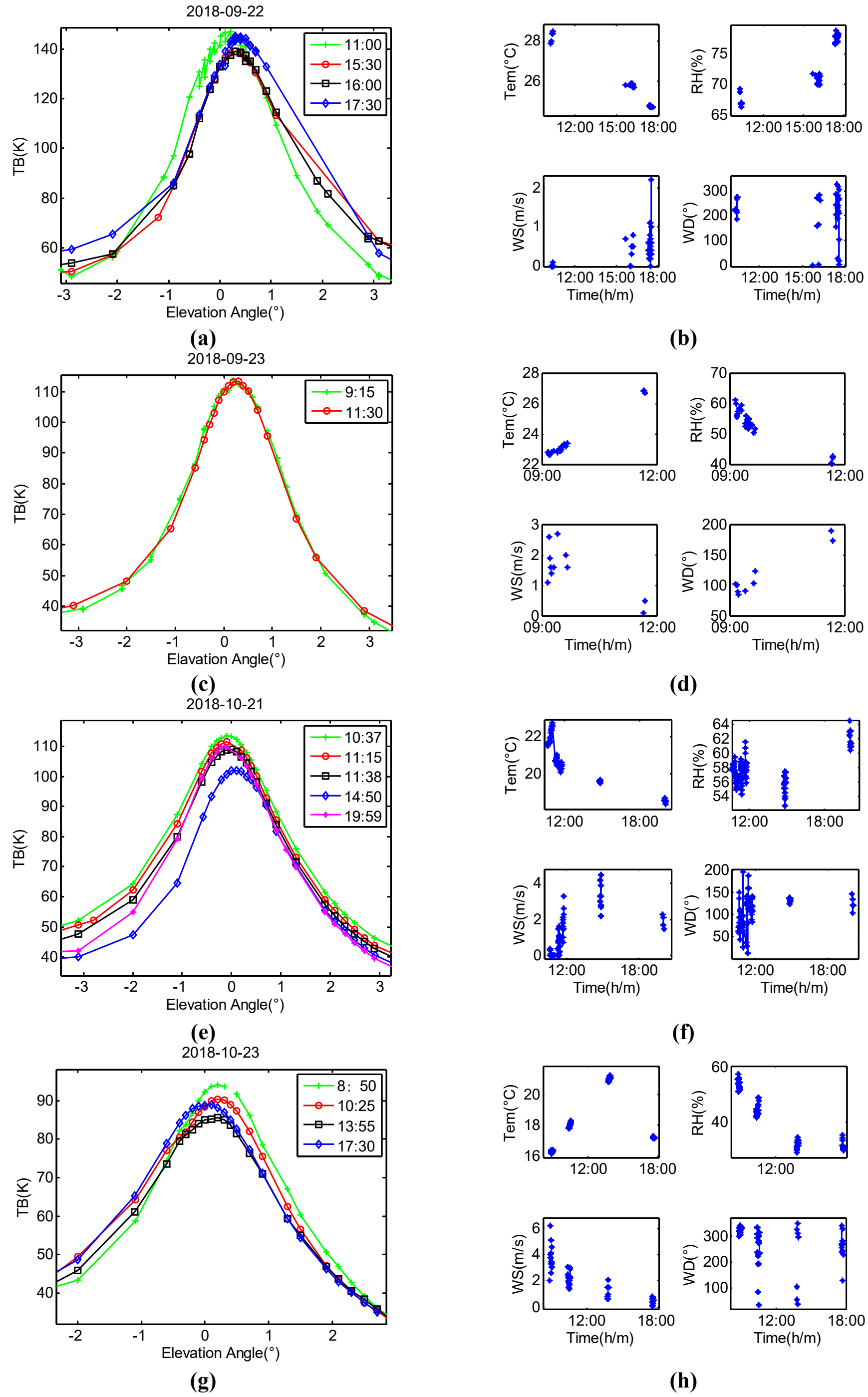

Figure 3. Measured X-band horizon polarized low elevation angle brightness temperature (LEATB) data and meteorological data. (**a**), (**c**), (**e**), and (**g**) are the TB (brightness temperature) data measured on 22 September 2018, 23 September 2018, 21 October 2018, and 23 October 2018, respectively. All the times in the figures are local standard time (Beijing time). (**b**), (**d**), (**f**)**,** and (**h**) are the corresponding meteorological data measured on 22 September 2018, 23 September 2018, 21 October 2018, and 23 October 2018, respectively. Four meteorological data are shown in each subfigure: temperature (upper left), relative humidity (upper right), wind speed (lower left), and wind direction (lower right).

3.1. Variation Characteristics with Elevation Angles

The measured TB at low elevation angles only contained the atmospheric radiation component when the microwave radiometer antenna beam did not reach the sea surface [27]. The 3 dB antenna beam width of the radiometer used in this paper was 1.1°, and the elevation angle above 0.6° usually only contain atmospheric downwelling radiation components, expressed as

$$Tb_{\text{downwelling}}(\theta)|_{H_0} = \tau(\theta, H_0, H)T_c + \int_{H_0}^{H} dhcsc\theta\alpha(h)T_a(h)\tau(\theta, H_0, h) \tag{10}$$

$$\tau(\theta, h_1, h_2) = \exp\left[-\int_{h_1}^{h_2} dhcsc\theta\alpha(h)\right] \tag{11}$$

The first term in Equation (10) represents the attenuated cosmic radiation where the cosmic radiation Tc = 2.76 K, H_0 is the height at which the downwelling brightness temperature is measured, and H is the height of the top of the atmosphere. The transmittance function given by Equation (11) is the atmospheric transmittance for radiation from h_1 to h_2 along a slant path that makes an angle θ with the horizontal plane. The second term in Equation (10) represents the integrated downwelling atmospheric emission, where $\alpha(h)$ and $T_a(h)$ are the absorption coefficient and temperature of the atmosphere at height h, respectively. In a sunny day, $\alpha(h)$ can be expressed as follows

$$\alpha(h) = \alpha_{H_2O}(h) + \alpha_{O_2}(h) \tag{12}$$

While in a cloudy day, $\alpha(h)$ can be expressed as follows

$$\alpha(z) = \alpha_{H_2O}(h) + \alpha_{O_2}(h) + \alpha_{\text{liquid}}(h) \tag{13}$$

where $\alpha_{H_2O}(h)$, $\alpha_{O_2}(h)$, $\alpha_{\text{liquid}}(h)$ are the absorption coefficient of water vapor, oxygen, and liquid water, respectively.

When the antenna beam reached the sea surface, the measured TB was the upwelling TB scattered from the sea surface. Considering the sea surface scattering, the h-polarized upwelling brightness temperature at the sea surface $Tb_{upwelling}(\theta_0, \varphi_0, \varepsilon_{//})\big|_0$ could be expressed as [27]

$$\begin{gathered} Tb_{upwelling}(\theta_0, \varphi_0, \varepsilon_{//})|_0 \\ = E(\theta_0, \varphi_0, \varepsilon_{//})T_s \\ +(4\pi sin\theta_0)^{-1} \int_{2\pi} d\Omega_s Tb_{i,j}|_0 \cdot [\delta(\theta_i, \varphi_i, \varepsilon_{//}; \theta_0, \varphi_0, \varepsilon_{//}) \\ +\delta(\theta_i, \varphi_i, \varepsilon_{\perp}; \theta_0, \varphi_0, \varepsilon_{//})] \end{gathered} \tag{14}$$

On the right side of Equation (14), the first term represents the sea surface emission component, where $E(\theta_0, \varphi_0, \varepsilon_{//})$ is the sea surface emission coefficient at an elevation angle θ_0 and an azimuth angle φ_0 in a horizontal polarization $\varepsilon_{//}$, and T_s is the sea surface temperature in Kelvin. The second term represents the sea surface scattering component of the atmospheric radiation TB, where $\varepsilon_{\perp}$ is vertical polarization, $Tb_{i,j}\big|_0$ is the ambient downwelling brightness temperature at the surface in the direction of (θ_i,φ_i), and the term $\delta(\theta_i, \varphi_i, \varepsilon_{//}; \theta_0, \varphi_0, \varepsilon_{//})$ is the bistatic normalized radar cross-section (NRCS) for horizon polarized radiation incident along the direction of an elevation angle θ_i and an azimuth angle φ_i and horizon polarized radiation scattered along (θ_0, φ_0). The another NRCS in Equation (14) is for scattered vertical polarized radiation $Tb_{i,j}\big|_0$. The scattering signal in Equation (14) is conducted over all differential solid angles ($d\Omega_s$) in the upper hemisphere of 2π steradians. Therefore, $Tb_{\text{upwelling}}(\theta_0, \varphi_0, \varepsilon_{//})\big|_{H_0}$ the upwelling brightness temperature measured at height H_0 ($Tb_{\text{upwelling}}(\theta_0, \varphi_0, \varepsilon_{//})\big|_{H_0}$) could be expressed as Equation (15).

$$\begin{aligned} & Tb_{\text{upwelling}}(\theta_0, \varphi_0, \varepsilon_{//})|_{H_0} \\ & = \tau(\theta_0, 0, H_0) Tb_{\text{upwelling}}(\theta_0, \varphi_0, \varepsilon_{//})|_0 \\ & + \int_0^{H_0} dh csc\theta_0 \alpha(h) T_a(h) \tau(\theta_0, h, H_0) \end{aligned} \tag{15}$$

The first term in Equation (15) represents the TB component driven by surface emission and scattering, which is attenuated by the transmittance $\tau(\theta_0, 0, H_0)$ for radiation from the sea surface to the observation point H_0 along a slant path that makes an angle θ_0 with the horizontal plane, as shown in Equation (13). The second term in Equation (15) represents the TB component driven by integrated upwelling atmospheric emission.

The measured LEATB data of the X-band with the horizontal polarization are shown in Figure 3. As the LEATB showed an arched pattern when the elevation angle ranged from 3° to −3°, this study defined ϕ_{TBmax} as the elevation angle when TB reached the maximum value. Since a ground-based microwave radiometer antenna with the 3 dB beam width of 1.1° was used in this experiment, the sea surface effect on the measured TB at elevation angle higher than 0.6° could be discarded, and consequently, the atmospheric downwelling TB was contained in the measured TB. The small atmospheric absorption at the X-band corresponded to a small TB value at the X-band at high elevation angles. As the elevation angle was reduced from 3° to 1°, the TB increased due to a longer path and a larger optical thickness of the downwelling radiation. In addition, the maximum value of the weight function moved downward along with the height as the elevation angle decreased, and then the weight of the lower atmosphere increased. Such a mechanism might cause an increase in the TB measurements as the temperature and humidity in the lower atmosphere were generally higher than those in the upper atmosphere. In addition, normally, the near sea haze had lots of large hydrometeors, which could enlarge the absorption coefficient of the atmosphere, as shown in Equations (12) and (13), so it could enlarge the atmospheric downwelling TB component in X-band and cause an increase in the TB measurements. When the elevation angle was reduced from ϕ_{TBmax} to −3°, the measured X band horizontal polarized upwelling TB data ($Tb_{\text{upwelling}}(\theta_0, \varphi_0, \varepsilon_{//})\big|_{H_0}$) decreased rapidly, as shown in Figure 3. In Equation (14), the upwelling TB at the sea surface was a function of the NRCS (δ), the sea surface emissivity (E), and the atmospheric downwelling TB, which were also determined corresponding to the elevation angle. Under the assumption of thermal equilibrium, Kirchhoff's law allowed the emissivity to be expressed as an integral of the NRCS

$$\begin{aligned} E(\theta_0, \varphi_0, \varepsilon_{//}) = \quad & 1 - (4\pi\theta_0)^{-1} \int_{2\pi} d\Omega_s \cdot [\delta(\theta_i, \varphi_i, \varepsilon_{//}; \theta_0, \varphi_0, \varepsilon_{//}) \\ & + \delta(\theta_i, \varphi_i, \varepsilon_{\perp}; \theta_0, \varphi_0, \varepsilon_{//})] \end{aligned} \tag{16}$$

As the elevation angle (θ_0) ranged from ϕ_{TBmax} to −3°, the X band horizontal polarized sea surface emissivity was small and gradually increasing [28]. For a flat specular sea surface, the atmospheric radiation scattered in a direction $\vec{k}_0$ was solely driven by the reflection of downwelling radiation incident along the propagation vector $\vec{k}_r$.

$$\vec{k}_r = \vec{k}_0 - 2\left(\vec{k}_0 \cdot \vec{r}\right)\vec{r} \tag{17}$$

where $\vec{r}$ is the earth radius vector normalized to unit length. For a rough sea surface, the downwelling radiation was scattered in a variety of directions, which was primarily driven by an incident power coming from a cone centered on $\vec{k}_r$ for the power scattered in direction $\vec{k}_0$. The width of the cone was enlarged with surface roughness [27]. The atmospheric downwelling radiation TB ($Tb_{i,j}$) in the direction (θ_s, φ_s) had a rapid inverse proportion to the elevation angle (θ_s). Therefore, the elevation angle of the propagation vector $\vec{k}_r$ increased as the elevation angle θ_0 decreased from ϕ_{TBmax} to −3°, which caused a rapid decrease in the downwelling radiation ($Tb_{i,j}$) in Equation (14). For the elevation range between ϕ_{TBmax} and −3°, the downwelling radiation of the atmosphere on the sea surface ($Tb_{i,j}\big|_0$) was much larger than the sea surface radiation, $E(\theta_0, \varphi_0, \varepsilon_{//})T_s$, and consequently, the second term on the right side of Equation (14) plays a major role in determining the total upwelling TB at the sea surface $Tb_{upwelling}(\theta_0, \varphi_0, \varepsilon_{//})\big|_0$. In other words, $Tb_{i,j}\big|_0$ decreased rapidly along with the decrease in elevation angle from ϕ_{TBmax} to $-3°$, while the sea surface emission coefficient $E(\theta_0, \varphi_0, \varepsilon_{//})$ and the bistatic NRCS changed slowly, resulting in a rapid decrease in the upwelling TB at the sea surface ($Tb_{upwelling}(\theta_0, \varphi_0, \varepsilon_{//})\big|_0$). Therefore, the X-band horizontal polarized upwelling TB within the elevation angle interval between −3° and +3° had a shape of the arch, and the TB was large in the middle and small at both sides.

3.2. Temperature and Humidity Effects on the LEATB

Under all fixed parameters except for atmospheric temperature in the radiative transfer equation, the LEA atmospheric radiation TB increased as the atmospheric temperature increased. Such a relationship could be similarly applied for atmospheric humidity, i.e., the atmospheric radiation TB increased as the atmospheric humidity increased, while the effect of the atmospheric pressure on the atmospheric radiation TBs was small [21].

As shown in Figure 3a,b, the relative humidity on 22 September 2018 became larger over time, i.e., 11:00 < 15:30 < 16:00 < 17:30 (all the times here are local standard time), and the horizontally polarized LEATBs at elevation angles higher than ϕ_{TBmax} showed the highest values at 16:00 and 15:30 (similar to each other) and the smallest at 11:00, indicating that the TB had a proportional relationship to the relative humidity and the atmospheric temperature. For example, the TB at 11:00 was smaller than those at 17:30, 16:00, and 15:30 due to the less relative humidity. In addition, the atmospheric radiation TB at 17:30 was smaller than those at 16:00 and 15:30 due to the lower atmospheric temperature. As the variation of the relative humidity was relatively smaller than that of the atmospheric temperature, the TB was influenced more by the atmospheric temperature. From the data at elevation angles higher than ϕ_{TBmax} on 22 September 2018, it was found that the LEATB sensitively corresponded to the changes in the atmospheric parameter profiles. Figure 3c,d shows the measurement on 23 September 2018. The observed TB at the elevation angles $\phi > \phi_{TBmax}$ was a steady status from 9:15 to 11:30, mainly due to a trade-off effect between the relative humidity and temperature on the TB. On 21 October 2018, in Figure 3e,f, on the contrary, the variation of the atmosphere temperature induced the change in the atmospheric TB observations as the relative humidity was a steady status from 10:37 to 14:50. The tradeoff effect between the relative humidity and temperature from 14:50 to 19:59 resulted in relatively stable LEATBs, as shown in Figure 3e. On 23 October 2018, in Figure 3g,h, the TB observations decreased over time, i.e., 8:50 > 11:25 > 13:55, which corresponded to the change in the relative humidity rather than that in the temperature (8:50 < 11:25 < 13:55), indicating that the relative humidity was a primary driver for the TB during this time. The atmospheric TBs at LEAs did not exhibit much change from 13:55 to 17:30 due to the tradeoff effect between the relative humidity and the temperature.

These results indicated that the sensitivity of the atmospheric TB at the low elevation angles was stronger than that at higher elevation angles. For example, the TB variation at the elevation angle of 3° in a day could reach more than 10 K, and the variation in other days could reach more than 20 K. In addition, both the atmospheric temperature and relative humidity had a significant impact on the X-band absorption coefficient and the X-band TBs.

3.3. Wind Effects on LEATBs

In this section, the variation of the horizontally polarized LEATB with wind speed was investigated based on the observed data. Since the LEATB data obtained during the experiment under low sea state, the data-based analysis in this section was only applicable to low sea conditions. As shown in Figure 3a,b, the atmospheric LEATB in the elevation angle interval of [1, 3] at 11:00 am 22 September 2018 was the smallest among those at 11:00, 15:30, 16:00, and 17:30, while the LEATBs at the left side of ϕ_{TBmax}, $(-2 \sim \phi_{TBmax})$ were the biggest. This result might be caused by the wind speed that plays a major role in the variation of the upwelling TB. When the wind speed became smaller, for instance, the TB observations at the left side of ϕ_{TBmax} became larger. Comparing the observed data at 15:30, 16:00, and 17:30, the decreases in the TB observations were small when the wind speed ranged from approximately 0 m/s to 1 m/s. As shown in Figure 3c,d, the wind speed from 9:15 to 11:30 on 23 September 2018 varied from 1.5 m/s to 0.5 m/s. The observed values on both sides of the elevation ϕ_{TBmax} did not change, indicating that the atmospheric radiation, sea surface scattering, and emission had little change during that period. On 21 October 2018, the relative sizes of the atmospheric radiation TBs at 10:37, 11:15, 11:38, 14:50, 19:59 decreased over time, i.e., 10:37 > 11:15 > 11:38 > 14:50 > 19:59, while the relative sizes of the wind speed mostly increased, i.e., 10:37 < 11:15 < 11:38 ≈ 19:59 < 14:50, as shown in Figure 3e,f. The upwelling TB at 14:50 was significantly smaller than those at others, while the wind speed at 14:50 was the largest (average wind speed of 3 m/s). These results indicated that the LEATB at the left side of ϕ_{TBmax} decreased under wind speeds higher than 1.5 m/s, while the decrease in the LEATBs at the left side of ϕ_{TBmax} caused by the sea surface scattering was not obvious, given that the mean wind speed was within 0 m/s to 1.5 m/s, as shown in Figure 3e,f. On 23 October 2018, in Figure 3g,h, the mean wind speed was 4.5 m/s at 8:50, 2 m/s at 10:25, 3 m/s at 13:55, and 0.5 m/s at 17:30. The atmospheric LEATB at 8:50 was the maximum, while the left side of the scanning TB data at 8:50 was the minimum, which was caused by the increase in wind speed that led to a decrease in the left side of the LEATB data. Similarly, the atmospheric radiation TB at 10:25 was larger than that at 17:30, and the left side of the scanning TB data at 10:25 was smaller than that at 17:30. These results were also induced by the fact that the wind speed at 10:25 was higher than that at 17:30. Comparing with the observed LEATB data at 13:55 and 17:30, there was no significant difference between them on the right side of the LEATB data, while the LEATB at the left side at 13:55 was less than that at 17:30, which was also affected by the higher wind speed at 13:55.

From the analysis above, it was prominent that the TBs at the elevation angle less than ϕ_{TBmax} were considerably affected by wind speed. Given other fixed parameters, the left side LEATB data was not affected under the wind speed between 1 and 1.5 m/s, while the left side LEATB data was effected considerably under the wind speed larger than 2 m/s; as the wind speed increased, the left side of the LEATB data decreased obviously.

From Equation (14) that expresses the upwelling brightness temperature at the sea surface, the horizontal polarized sea surface emission coefficient $E(\theta_0, \varphi_0, \varepsilon_{//})$ increased as the wind speed over the sea surface increased. Since the sea surface temperature (T_s) had a small diurnal fluctuation, the sea surface radiation component $E(\theta_0, \varphi_0, \varepsilon_{//})T_s$ became larger [29,30]. The sea surface scattering increased as the wind speed at the sea surface increased [31–33]. As mentioned in Section 3.1, the power scattered in the direction $\vec{k}_i$ was primarily driven by an incident power coming from a cone centered on $\vec{k}_r$, and the width of the cone increased with surface roughness. Therefore, an increase in the sea surface scattering and the width of the cone led to an increase in the weight of the higher elevation angle atmospheric radiation component in the integral of Equation (15), resulting in a decrease in the total weighted downwelling radiation

$$\left(4\pi sin\theta_0\right)^{-1}\int_{2\pi} d\Omega_s Tb_{i,j}|_0 \cdot \left[\delta(\theta_s, \varphi_s, \varepsilon_{//}; \theta_0, \varphi_0, \varepsilon_{//}) + \delta(\theta_s, \varphi_s, \varepsilon_{\perp}; \theta_0, \varphi_0, \varepsilon_{//})\right] \tag{18}$$

As the coefficient of the horizontally polarized sea surface emission and scattering in the elevation angle interval of $[-2, \phi_{TBmax}]$ were not sensitive to the wind speed, the decrease in the total weighted downwelling radiation might play an important role in a decrease in the total upwelling TB at the sea surface $Tb_{upwelling}(\theta_0, \varphi_0, \varepsilon_{//})\big|_0$.

The change rate of sea surface emission (E) was small with the elevation angles within the interval of [−1°, −2°], while the decreasing rate of the atmospheric downwelling TB ($Tb_{\text{downwelling}}(\vec{k}_r)|_0$) with the elevation angles at the sea surface was large, indicating that $Tb_{\text{downwelling}}(\vec{k}_r)|_0$ was a primary driver in the total upwelling TB $Tb_{\text{upwelling}}(\theta_0, \varphi_0, \varepsilon_{//})\big|_{H_0}$. Therefore, the total upwelling TB decreased under the elevation angle θ_0 within the interval of [−1°, −2°]. However, such a characteristic in the total upwelling

TB was not preserved when the elevation θ_0 of the X-band horizontally polarized TB at the height of H_0 $(Tb_{\text{upwelling}}(\theta_0, \varepsilon_{//})\big|_{H_0})$ decreased from −2° to −10°. When the elevation angle decreased gradually from −2° to −10°, the sea surface emissivity (E) increased gradually, and the corresponding downwelling atmospheric TB in the direction of $\vec{k}_r$ decreased accordingly. From Equation (17), one could find that the elevation angle of $\vec{k}_r$ (θ_r) was the negative of θ_0. From Figure 4, further, the changing rate of the atmospheric downwelling TB at the height H_0 radually decreased with the elevation angles within the interval of [1°, 10°]. Ignoring the height of H_0, it could be found that the change rate of the atmospheric downwelling TB at the sea surface decreased gradually with the elevation angle in the interval of 1° to 10°. When the elevation angle θ_0 decreased from −5° to −10°, the corresponding elevation angle θ_r of the atmospheric downwelling TB in direction $\vec{k}_r$ increased from 5° to 10°. The change rate of the atmospheric downwelling TB in $\vec{k}_r$ direction decreased gradually as the elevation angle θ_0 decreased from −5° to −10°. In contrast, the sea surface emission gradually increased with the elevation angles, resulting in a downward trend of the total upwelling TB $Tb_{\text{upwelling}}(\theta_0, \varphi_0, \varepsilon_{//})\big|_{H_0}$, as shown in Figure 4. In addition, the total upwelling TB $(Tb_{\text{upwelling}}(\theta_0, \varphi_0, \varepsilon_{//})\big|_{H_0})$ in the elevation angle interval of −1° to −2° at 8:50 was less than that at 17:30 (refer to Figure 4), while the total upwelling TB near the elevation angle of −10° at 8:50 was greater than that at 17:30. These results were caused by the fact that, in the elevation interval of −1° to −2°, the weight change of the atmospheric downwelling LEATBs induced by the increase of the sea surface roughness led to the decrease of the total weighted atmospheric downwelling TB at the sea surface $Tb_{\text{downwelling}}(\vec{k}_r)|_0$, consequently resulting in the decrease in the total upwelling TB $Tb_{\text{upwelling}}(\theta_0, \varphi_0, \varepsilon_{//})\big|_{H_0}$. In the elevation angle interval of [−5°, −10°], the change rate of the atmospheric downwelling TB ($Tb_{\text{downwelling}}(\vec{k}_r)|_0$) to the elevation angle became stagnant, given that the wind speed increased, resulting in a stagnant rate in the reduction of the total weighted atmospheric downwelling TB. Therefore, an increase in the sea surface emission induced by increasing the wind speed was a primary driver to determine the total upwelling TB at the height H_0 $Tb_{\text{upwelling}}(\theta_0, \varphi_0, \varepsilon_{//})\big|_{H_0}$. At the elevation interval of −5° to −10°, consequently, the higher wind speed might cause the larger total X band horizontal polarization upwelling TB at the sea surface $(Tb_{\text{upwelling}}(\theta_0, \varphi_0, \varepsilon_{//})\big|_0)$, which was consistent with the measurements of satellite-borne radiometers.

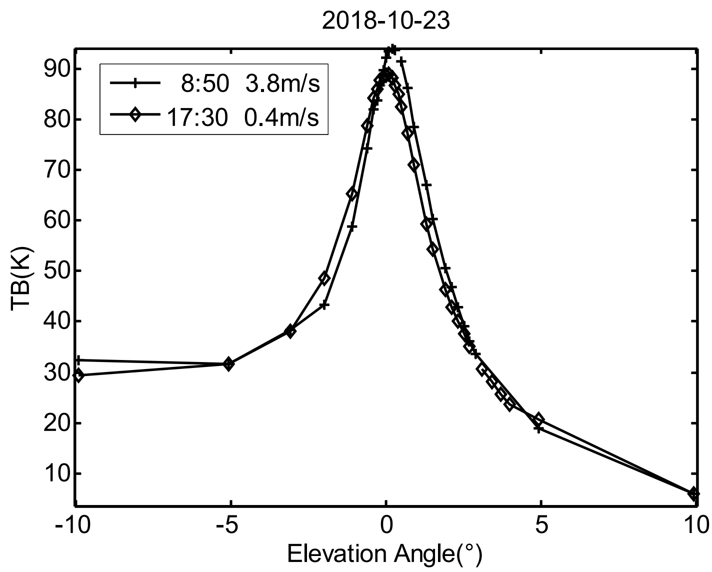

Figure 4. Measured data of the X-band horizontal polarization upwelling TBs against the elevation angles. The pluses in the figure are the TB data measured at 8:50 on 23 October 2018, and the diamonds in the figure are the TB data measured at 17:30 on the same day. The average wind speeds at 8:50 and 17:30 were 3.8 m/s and 0.4 m/s, respectively.

When under high sea state, for the X band horizontal polarization upwelling radiation TB, the sea surface emissivity became larger, almost like a blackbody, due to the large-scale sea surface slant and foam generated by sea surface wind. Under high sea state, if the sea surface emissivity E increased rapidly with wind speed, the first term on the right of Equation (14) may play a major role in the upwelling radiation TB at the sea surface $Tb_{\text{upwelling}}(\theta_0, \varphi_0, \varepsilon_{//})\big|_0$. Under this condition, a higher wind speed might cause a larger $Tb_{\text{upwelling}}(\theta_0, \varphi_0, \varepsilon_{//})\big|_0$, and the relationship between the LEATB and the sea surface wind speed obtained in this section, which was applicable to low sea state, was not applicable to the high sea state. The relationship between the X band horizontal polarization upwelling TB at the sea surface $Tb_{\text{upwelling}}(\theta_0, \varphi_0, \varepsilon_{//})\big|_0$ and the sea surface wind speeds under high sea state need to be further studied based on the measured data under high sea state.

3.4. Variation of LEATB Difference with a Change in OTHDC

Many studies have shown that, under certain meteorological conditions, the ship-borne microwave radar can see the targets beyond the line-of-sight due to a marine atmospheric duct that is capable of over-the-horizon detection. The atmospheric duct is an anomalous atmospheric refraction structure that significantly influences the propagation of ultrashort waves and microwaves in the marine atmosphere. Given that microwaves are trapped in the duct to form an over-the-horizon propagation, the detection capability of microwave radar can be greatly improved [34–36]. As in Equation (A1), an atmospheric duct is formulated once the gradient of the modified atmospheric refractivity in altitude is less than 0. The atmospheric ducts are usually classified into evaporation ducts, surface ducts, and suspended ducts, depending on their formation mechanism and morphology. Although the evaporation duct occurrence in the global ocean accounts for up to 90%, surface and suspended ducts are also important factors to be capable of over-the-horizon detection. In 1990, Paulus investigated the effects of the evaporation ducts on radar sea clutter and found that the evaporation ducts significantly increased the maximum range of radar sea clutter [37]. As a marine atmospheric duct often occurs from an abnormal distribution in the lower atmosphere, the microwave radiation LEATBs is likely to contain the distribution information on the lower atmosphere in altitude. Moreover, the atmospheric ducts affect the atmospheric LEATBs by causing abnormal deflection of the propagation path of the microwave radiation at low elevation angles, indicating that LEATB may contain the atmospheric duct information.

Employing the difference of LEATB between different elevation angles, the variation characteristics of the LEATB difference were analyzed to understand the impacts of the over-the-horizon detection capability (OTHDC). The radar's OTHDC was characterized by the farthest distance of radar sea surface echo (R_{max}) that was obtained in the 2018 Qingdao sea area measurement campaign. The variation of the microwave radiation brightness temperatures at low elevation angles was analyzed based on the observed TB data. Further, the variation of the atmosphere and atmospheric duct during the experiments was also examined based on the observed and meteorological parameters (temperature, humidity, pressure, sea surface wind speed, and wind direction) and simulated meteorological parameters from weather research and forecasting (WRF) model.

In order to identify the correlation between the LEATB difference and the OTHDC, trend analysis on the LEATB difference was conducted during the periods when the farthest distance of the sea surface echo data (R_{max}) changed in a day. As the influence of the sea surface scattering and emission could be neglected if the elevation angle was above 0.6° due to the 3-dB beam width of the radiometer (1.1°), it could be considered that the observed LEATB data only contained the atmospheric TB component. The physical mechanism of the correlation between the LEATB and the atmospheric duct was analyzed based on the data in the daytime to alleviate unexpected distortion in an analysis by a few numbers of night-time data.

Figure 5 shows the LEATB difference and OTHDC. In Figure 5a, the R_{max} varied from 310 km to less than 40 km at 15:30 to 17:30 on 22 September 2018. At a time, the TB difference between $TB(0.6°)$ and $TB(3.1°)$. increased from approximately 70 K to 95 K. In Figure 5b, the R_{max} between 9:15 and 11:30 on 23 September 2018 was constantly about 40 km, and a range of the TB difference was less than 2 K. The observed TB differences on 23 October 2018 are shown in Figure 5c. The R_{max} between 10:25 and 13:55 increased from 140 km to 200 km, and at a time, the TB difference between $TB(0.9°)$ and $TB(3.1°)$ decreased from approximately 48 K to 43 K. These results indicated that the LEATB difference was significantly affected by the change in the OTHDC during the daytime.

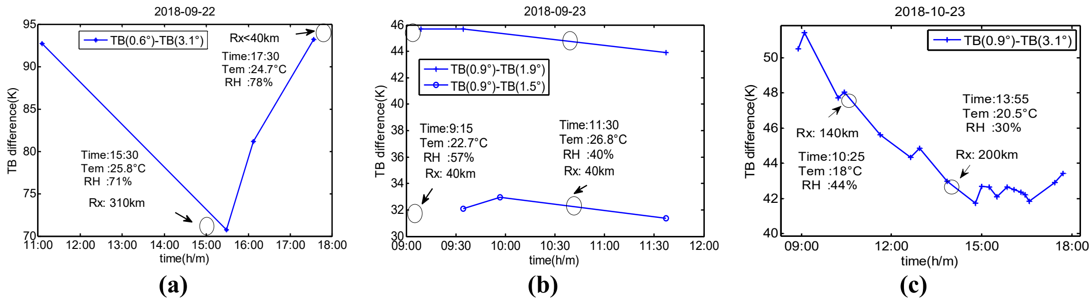

Figure 5. Observed LEATB difference and over-the-horizon detection capability (OTHDC). (**a**–**c**) on 22 September 2018, 23 September 2018, and 23 October 2018, respectively. The LEATB difference was obtained by the difference between the LEATB data at two elevation angles. For example, the LEATB difference between $TB(0.6°)$ and $TB(3.1°)$ in (**a**) represents the difference between the LEATB values at elevation angle 0.6° and 3.1°. The *Rmax* is the maximum range of radar echoes. The 'Time', 'Tem', and 'RH' represent local standard time (Beijing time), temperature, and relative humidity, respectively.

Figure 6 shows the evaporation ducts, on 22 and 23 September 2018 and 23 October 2018, simulated by the Navy Postgraduate School (NPS) evaporation duct model [38,39]. Figure A1 shows the influences of the wind speed and the atmospheric relative humidity on the evaporation ducts using outputs of the NPS model. Because the sea surface temperature, an essential parameter for the NPS model, had not been observed during the experiment, the sea surface temperature was set a constant in a day, which might cause certain computational errors. As the NPS model also assumed the saturated humidity (relative humidity of 100%) at the sea surface, a larger atmospheric duct strength was induced by a large atmospheric refractivity at the sea surface, as shown on the right part of Figure 6a–c. Considering the systematic biases in the NPS model, this study conducted a qualitative analysis to alleviate the impacts of model biases on the analysis of the relative variation of atmospheric duct strength in a day. The weather research forecast (WRF) model was used to calculate the surface duct and the atmospheric refractivity profile on 22 and 23 September 2018 and 23 October 2018, as shown in Figure 7.

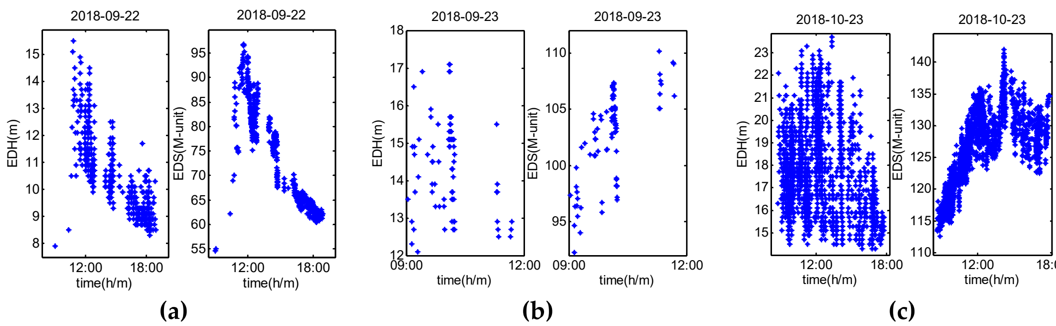

Figure 6. Time series of evaporation duct height (EDH) and evaporation duct strength (EDS) calculated by the Navy Postgraduate School (NPS) evaporation duct model. The data needed in the NPS model as input parameters were obtained by an automatic weather station (AWS). (**a**–**c**) show the evaporation duct on 22 September 2018, 23 September 2018, and 23 October 2018, respectively. In (**a**–**c**), the left part is the evaporation duct height (EDH) vs. time, and the right part is the evaporation duct strength (EDS) vs. time.

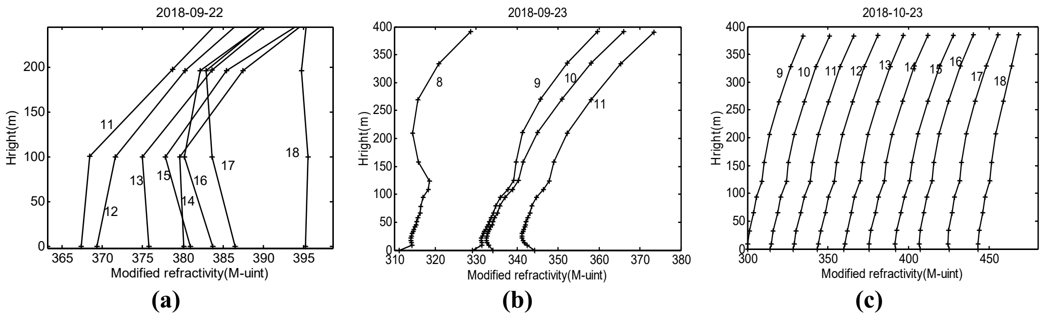

Figure 7. The atmospheric duct from the weather research and forecasting (WRF) data. The horizontal axis is the modified refractive index (M-unit), and the vertical axis is the height (m). (**a**–**c**) show the WRF data on 22 September 2018, 23 September 2018, and 23 October 2018, respectively. The numbers from 11 to 18 in the figures represent the local standard time for each atmospheric duct profile (i.e., 11:00 to 18:00). In order to improve the visualization of the modified refractivity profiles at different times in a day, the value of each modified refractivity profile was modified by $(n-10)\times 7$ M-units (**a**) and $(n-10)\times 15$ M-units (**b**,**c**) for the refractivity at n o'clock. For example, the refractivity at 11 and 18 o'clock modified 7 M-units and 56 M-units in (**a**), respectively.

In Figures 6a and 7a, both of the height and strength of the evaporation duct decreased from 11:00 to 18:00 on 22 September 2018, while the surface ducts from 11:00 to 15:30 gradually increased and bent down from 15:30 to 18:00. In addition, the evaporation duct at 15:30 became smaller, while the surface duct became larger at the time, indicating that the over-the-horizon detection was caused by the surface duct. At 18:00, a decrease in both the surface duct and the evaporation duct was observed, resulting in the disappearance of the over-the-horizon detection. In Figure 6b and 7b, the evaporation duct height between 9:00 and 11:00 on 23 September 2018 decreased slightly, while the evaporation duct strength increased. However, the surface duct was not changed significantly, resulting in a little change in over-the-horizon detection during this period. As shown in Figure 6c and 7c, there was no significant change in the evaporation duct height and the surface duct from 10:25 to 13:55 on 23 October 2018, while the evaporation duct strength increased gradually, indicating that the microwave over-the-horizon detection during this period was caused mainly by evaporation ducts.

The relationship between meteorological parameters (i.e., temperature, humidity, and pressure) and atmospheric ducts is shown in appendix A. As in Equation (A10), under a standard atmosphere, a temperature inversion should be greater or equal to 8.5 °C/100 m to generate an atmospheric duct, which is called temperature inversion. Equation (A11) represents that, under a standard atmosphere, the requirement to generate a duct is a humidity gradient less than or equal to −2.95 mb/100 m . This condition for the formation of a surface or an elevated duct is very hard to be reached neither by only temperature parameter anomaly in altitude nor by only humidity parameter anomaly. The atmospheric ducts are usually caused by the temperature inversion combined with a humidity plunge in altitude. Therefore, this study investigated the variation of the LEATB difference and the OTHDC to better understand the generation mechanism.

From the analysis above in this section, it was found that the over-the-horizon radar sea echoes at 15:30 on 22 September 2018 were caused by a surface duct. In Figure 5a, the atmospheric temperature over the sea surface decreased from 25.8 °C to 24.7 °C, and the relative humidity increased from 71% to 78%. The evaporation ducts are usually caused by an abrupt drop of the atmospheric humidity in altitude, while the surface ducts are caused by both an atmospheric temperature inversion and a drop of the atmospheric humidity in altitude. In this regard, the disappearance of the surface duct between 15:30 and 18:00 might be caused by the absence of the temperature inversion in the upper atmosphere, i.e., the temperature drop in the upper atmosphere was larger than that near the sea surface. As the TBs at a lower elevation angle were sensitive more to the lower atmosphere, $TB(0.6^{\circ})$ was affected by the lower atmosphere more than $TB(3.1^{\circ})$. Therefore, the difference of the variations between the upper and lower atmospheres might be dependent on the dramatic changes in the LEATB difference

$TB(0.6°) - TB(3.1°)$, as shown in Figure 5a. In Figure 5b, the OTHDC was stagnant from 9:15 to 11:30, and the TB difference varied less than 2 K. The observed temperature at 8 m ASL increased from 22.7 °C to 26.8 °C (i.e., 4.1 ° C), while the relative humidity decreased from 57% to 40% (i.e., a difference of 17%). As the NPS results shown in Figure 6b, the height of the evaporation duct (EDH) from 9:00 to 12:00 decreased, while the strength of the evaporation duct (EDS) increased. The decrease in the atmospheric duct height counteracted the increase of atmospheric duct strength, resulting in less influence on the OTHDC. In Figure 7b, there was no significant change in the surface duct from 9:00 to 11:00. The little variation of evaporation duct and surface duct during this period from 9:00 to 11:00 might lead to little change in the OTHDC. Further, the effects of increasing temperatures on the LEATBs were offset by a decrease in the relative humidity, causing little relative change between low and high altitudes, subsequently resulting in little change in the LEATB difference. As shown in Figure 5c, the maximum range of radar sea echo increased from 140 km to 200 km from 10:25 to 13:55 on 23 October 2018. At this time, the TB difference and the relative humidity decreased from 48 K to 43 K and 45% to 30%, while the temperature increased from $18°C$ to $21°C$, as shown in Figure 5c. The results of the NPS model showed that the strength of the evaporation duct during that period increased obviously, as shown in Figure 6c. Besides, the WRF model results illustrated that the variation of the surface duct was not prominent during that period, as shown in Figure 7c. These results indicated that the variation of the OTHDC was mainly caused by an increase in the evaporation duct. Based on the theory of the atmospheric boundary layer, the atmosphere from 10:25 to 13:55 was in a warming process in which the sea surface temperature rose faster than that of the upper atmosphere, causing a decrease in the humidity in the lower atmosphere faster than that in the upper atmosphere. This atmospheric warming process might result in different changing rates between the upper and lower atmospheres. The sensitivity of the TB at a lower elevation angle to the lower atmosphere also induced the variation of the TB difference $TB(0.9°) - TB(3.1°)$ during the period from 10:25 to 13:55, as shown in Figure 7c.

Overall, the results in this study showed that a change in the OTHDC influenced the LEATB difference significantly. A further study on the correlation between the atmospheric duct and the LEATB is necessary with more comprehensive observed data to better understand the mechanism.

4. Application

The conclusion is drawn in Section 3.3 that the total upwelling LEATB at the sea surface $Tb_{upwelling}(\theta_0, \varphi_0, \varepsilon_{//})\big|_0$ decreased when the wind speed increased. Therefore, the LEATB has a potential application for the remote sensing of sea surface wind speed [40]. Since the conclusion in Section 3.3 was only applicable to low sea state, the application and analysis here were also limited to the low sea state. For a rough sea surface, the downwelling radiation was scattered in a variety of directions. As a result, the power scattered in direction $\vec{k}_0$ was primarily due to incident power coming from a cone centered on $\vec{k}_r$. The width of the cone increased with surface roughness. The closed-form approximation was found by expanding the downwelling brightness temperature $Tb_{downwelling}\left(\vec{k}_s\right)\Big|_0$ about the propagation vector $\vec{k}_r$.

$$Tb_{downwelling}\left(\vec{k}_s\right)\Big|_0 = Tb_{downwelling}\left(\vec{k}_r\right)\Big|_0 + \Omega\left(\vec{k}_r, \vec{k}_s\right) \tag{19}$$

where $\Omega\left(\vec{k}_r, \vec{k}_s\right)$ is the variation of the downwelling brightness temperature relative to $Tb_{downwelling}\left(\vec{k}_r\right)\Big|_0$, which is given by Equation (10) with θ_r replacing θ (The propagation vector $\vec{k}_r$ and $\vec{k}_s$ ave an elevation angle θ_r and θ_s, respectively. For simplicity, the TBs with the same elevation angle but different azimuth angles in the main beam are considered as equal).

Substituting Equation (19) into (14) and utilizing the relationship (16) between the sea surface emissivity E and the NRCS yield

$$\begin{aligned}&Tb_{\text{upwelling}}(\theta_0, \varepsilon_0, \in_{//})|_0 \\ &= E(\theta_0, \varepsilon_0, \in_{//})T_S + [1 - E(\theta_0, \varepsilon_0, \in_{//})]Tb_{\text{downwelling}}\left(\vec{k}_r\right)\Big|_0 \\ &+ (4\pi sin\theta_0)^{-1} \int_{2\pi} d\vec{k}_s \Omega(\theta_r, \theta_s)[\delta(\theta_s, \varepsilon_s, \in_{//}, \theta_0, \varepsilon_0, \in_{//}) \\ &+\delta(\theta_s, \varepsilon_s, \in_{\perp}, \theta_0, \varepsilon_0, \in_{//})]\end{aligned} \tag{20}$$

Wentz's analysis showed that the integral in Equation (20) is approximately proportional to the friction velocity U_*, to the downwelling brightness temperature $Tb_{downwelling}\left(\vec{k}_r\right)\Big|_0$, and to the sea surface reflectivity $[1 - E(\theta_0, \varphi_0, \varepsilon_{//})]$. Hence, they approximated the diffuse scattering integral in Equation (20) by

$$I_\Omega = \omega U_* \cdot Tb_{downwelling}\left(\vec{k}_r\right)\Big|_0[1 - E(\theta_0, \varphi_0, \varepsilon)] \tag{21}$$

where ω is the coefficient. Wentz's analysis was based on five wind states ranging in friction velocities from 0.2 m/s to 1 m/s, and the low sea state with friction velocities lower than 0.2 m/s was not taken into account. In this paper, Equation (21) was still used to represent the diffuse scattering integral in Equation (20) under low sea state, and the validity of this approximation would be verified by the measured data at the end of this chapter.

Substituting Equations (20) and (21) into (15), Wentz [31] derived a formula of the upwelling brightness temperature measured at altitude H_0 as follows,

$$\begin{aligned}&Tb_{\text{upwelling}}(\theta_0, \varepsilon_{//})|_{H_0} \\ &= \tau(\theta_0, 0, H_0)\Big\{E(\theta_0, \varepsilon_{//})T_s + (1 + \omega U_*)[1 \\ &-E(\theta_0, \varepsilon_{//})]\, Tb_{\text{downwelling}}\left(\vec{k_r}\right)\Big|_0\Big\} + \int_0^{H_0} dhcsc\theta_0 \alpha(h) T_a(h) \tau(\theta_0, h, H_0)\end{aligned} \tag{22}$$

$$Tb_{\text{downwelling}}\left(\vec{k_r}\right)|_0 = \tau(\theta_r, 0, H)T_c + \int_0^H dhcsc\theta_r \alpha(h) T_a(h) \tau(\theta_r, 0, h) \tag{23}$$

In Equation (22), the first term on the right side represents the components of the upwelling TB at the sea surface and attenuated by the atmospheric transmittance $\tau(\theta_0, 0, H_0)$. The second term is the atmospheric upwelling TB component from the sea surface to the height H_0 along an oblique path with an elevation angle of θ_0. U_* is the friction velocity, ω is the coefficient of U_*, $[1 - E(\theta_0, \varepsilon_{//})]$ is the sea-surface reflectivity, $Tb_{\text{downwelling}}\left(\vec{k_r}\right)\Big|_0$ is the downwelling brightness temperature at the sea surface. Equation (23) is derived by the fact that the incidence angle θ_r equals θ_0 according to Equation (17).

Substituting Equation (21) into (20), the upwelling brightness temperature at the sea surface could be obtained,

$$Tb_{\text{upwelling}}(\theta_0, \varepsilon_{//})|_0 = E(\theta_0, \varepsilon_{//})T_s + (1 + \omega U_*)[1 - E(\theta_0, \varepsilon_{//})]Tb_{\text{downwelling}}\left(\vec{k_r}\right)|_0 \tag{24}$$

As H_0 was small (e.g., 8 m ASL in this study) for shore-based or shipborne microwave radiometers, the atmospheric absorption from sea level to an altitude H_0 could be ignored in the following analysis. From Equations (22) and (24), thus, Equation (25) could be obtained as follow,

$$Tb_{\text{upwelling}}(\theta_0, \varepsilon_{//})\Big|_{H_0} \approx Tb_{\text{upwelling}}(\theta_0, \varepsilon_{//})\Big|_0 \tag{25}$$

According to the analysis in Section 3.3, it was found that the X band horizontal polarization upwelling LEATB $Tb_{\text{upwelling}}(\theta_0, \varepsilon_{//})\Big|_{H_0}$ under low sea state was mainly affected by the second term in Equation (24) that is more sensitive to the change in wind speed.

Substituting Equation (24) into Equation (25), a simpler expression for the upwelling TB at altitude H_0 could be obtained, as shown in Equation (26).

$$Tb_{\text{upwelling}}(\theta_0, \varepsilon_{//})|_{H_0} \approx E(\theta_0, \varepsilon_{//})T_s + (1 + \omega U_*)[1 - E(\theta_0, \varepsilon_{//})]Tb_{\text{downwelling}}\left(\vec{k_r}\right)|_0. \tag{26}$$

where the sea surface emissivity (E) could be expressed as the sum of the emissivity (E_s) for a specular water surface and the total change in the emissivity due to roughness, wind direction, and foam ($\Delta\bar{E}$), as in Equation (27).

$$E = E_s + \Delta\bar{E} \tag{27}$$

The specular emissivity (E_s) was calculated by the Fresnel Equation as follows,

$$E_s = 1 - \left| \frac{\eta cos\theta_r - \left(\varepsilon - sin^2\theta_r\right)^{0.5}}{\eta cos\theta_r + \left(\varepsilon - sin^2\theta_r\right)^{0.5}} \right|^2 \tag{28}$$

where ε is the sea water dielectric constant, and the parameter η equals either unity for h-pol or ε for v-pol.

The expression of U_* could be derived from Equation (26) as follows,

$$U_* \approx \frac{1}{\omega\cdot\left[1-E\left(\theta_0,\varepsilon_{//}\right)\right]} \cdot \frac{Tb_{\text{upwelling}}\left(\theta_0,\varepsilon_{//}\right)|_{H_0}}{Tb_{\text{downwelling}}\left(\vec{k_r}\right)\Big|_0} - \frac{1}{\omega} \cdot \frac{E\left(\theta_0,\varepsilon_{//}\right)}{\left[1-E\left(\theta_0,\varepsilon_{//}\right)\right]} \cdot \frac{T_s}{Tb_{\text{downwelling}}\left(\vec{k_r}\right)\Big|_0} - \frac{1}{\omega} \tag{29}$$

The sea surface emissivity value at low elevation angles was much smaller than 1, i.e., $E << 1$ and then $E/(1 - \text{E}) << 1$. Thereby, the atmospheric downwelling TB at the sea surface $Tb_{\text{downwelling}}\left(\vec{k_r}\right)\Big|_0$ became very large. Therefore, the second term on the right side of Equation (29) is much smaller than the value of the third term, and consequently, Equation (29) could be simplified as

$$U_* \approx \frac{1}{\omega \cdot [1 - E(\theta_0, \varepsilon_{//})]} \cdot \frac{Tb_{\text{upwelling}}(\theta_0, \varepsilon_{//})\big|_{H_0}}{Tb_{\text{downwelling}}\left(\vec{k_r}\right)\Big|_0} - \frac{1}{\omega} \tag{30}$$

According to the analysis in Section 3.3, it was found that, under low sea state, the second term on the right side of Equation (24) was more sensitive to the change in wind speed than the first term.

That is, the sea surface emissivity (E) had a smaller influence on the upwelling TB $Tb_{\text{downwelling}}\left(\vec{k_r}\right)|_0$ than the second item on the right side of Equation (24) when the sea surface wind speed changed. Therefore, the total change in the emissivity due to both roughness and foam, $\Delta\bar{E}$, under low sea state could be ignored. In Equation (30), once set $A = \frac{1}{\omega\cdot\left[1-E\left(\theta_0,\varepsilon_{//}\right)\right]}$ and $B = -\frac{1}{\omega}$, then A and B become a constant coefficient. Therefore, Equation (30) could be expressed using A and B as follows,

$$U_* \approx A \cdot \frac{Tb_{\text{upwelling}}(\theta_0, \varepsilon_{//})|_{H_0}}{Tb_{\text{downwelling}}\left(\vec{k_r}\right)|_0} + B \tag{31}$$

By Equation (31), the friction velocity (U_*) was obtained from the TB ratio $Tb_{\text{upwelling}}(\theta_0, \varepsilon_{//})|_{H_0}/Tb_{\text{downwelling}}(\vec{k_r})|_0$. In other words, Equation (31) could be applied for remote sensing of the friction velocities based on the LEATBs using the constant coefficients A and B fitted by measured data $Tb_{\text{upwelling}}(\theta_0, \varepsilon_{//})|_{H_0}$, $Tb_{\text{downwelling}}(\vec{k_r})|_0$, and U_*. Sethu Ramon and Rayner [41] employed the experimental data in the case of the medium rough sea surface to derive an empirical formula of friction velocity from the average wind speed at an altitude of 6 m (U_6).

$$U_{*}= 0.033U_6 \tag{32}$$

In this paper, the observed data in the Qingdao sea area during the 2018 measurement campaign were used to fit the coefficients of A and B in Equation (31). During the experiment, an AWS was installed at an altitude of 6 m to measure essential meteorological parameters (i.e., temperature, humidity, and pressure). In addition, a microwave radiometer was fixed at an altitude of 8 m to obtain the X band horizontally polarized LEATB data. Since the AWS was deployed over the shore, the wind velocity might be slower than that over the sea winds, as well in wind direction. The application of Equation (32) to the Qingdao area, china, could also cause errors. However, the purpose of this chapter was to verify the feasibility of the remote sensing of the sea surface wind speed based on the LEATBs. The errors caused by wind speed measurement and Equation (32) would not affect the feasibility verification.

At low elevation angles, when the ground-based microwave radiometers were observed at a positive elevation angle, it was collecting noise also from the emission of the sea surface. Since the radiometer had a main beam aperture of 1.1 deg, this effect was mostly in the near side lobes or at negative elevations. Besides, when the ground-based microwave radiometers were observed at a negative elevation angle, it was collecting noise also from the atmospheric downwelling radiation in the near side lobes or at positive elevations. To avoid the interference of the atmospheric downwelling TB with the sea surface upwelling TB, TB with an elevation angle in the interval (-0.6, 0.6) should not be used as $Tb_{\text{upwelling}}$ or $Tb_{\text{downwelling}}$ in Equation (31).

In this chapter, the upwelling TB data measured at the elevation angle of -1 and the downwelling TB at the elevation angle of 1° were selected as $Tb_{\text{upwelling}}(-1, \varepsilon_{//})\big|_{H_0}$ and $Tb_{\text{downwelling}}(1)\big|_0$ in Equation (31), respectively, to obtain the specific coefficients of $A(-1, 1)$ and $B(-1, 1)$. It was prominent that the coefficients A and B were a function of the selected elevation angles of the upwelling and downwelling TBs. The wind speed data measured at an altitude of 6 m was used as U_6 in Equation (32) to calculate the friction velocity U_*, which was incorporated into Equation (31) to fit the coefficients $A(-1, 1)$ and $B(-1, 1)$.

The detailed steps for the fitting were as follows,

1. Pre-processing the measurement data and selecting the quality-controlled data.
2. Selecting the TB data, extracting the sea surface wind speed data (U_6) at the time of TB measurement, and calculating the 5-minute average wind speed $\bar{U}_6$.
3. Calculating the friction velocity U_* by Equation (32).
4. From a diagram of the friction velocity U_* against the TB ratio ($Tb_{\text{upwelling}}(\theta_0, \varepsilon_{//})|_{H_0}/Tb_{\text{downwelling}}(\vec{k_r})|_0$), a line with slope A $(-1, 1)$ and intercept B$(-1, 1)$ could be obtained by fitting the experimental data using Equation (31).

Using the measured data on 21 and 23 October 2018, a diagram was derived, as shown in Figure 8, where the blue circles represent the measured data. Figure 8 shows a linear relationship between the friction velocity U_* and the TB ratio ($Tb_{\text{upwelling}}(\theta_0, \varepsilon_{//})|_{H_0}/Tb_{\text{downwelling}}(\vec{k_r})|_0$). The results shown in Figure 8 indicated that the using of Equation (21) to represent the diffuse scattering integral in Equation (20) under low sea state was suitable. In particular, an inverse proportional relationship was consistent with the results in Section 3.3. By fitting the measured data using the least square method, a slope A $(-1, 1)$ of -0.1928 and an intercept B$(-1, 1)$ of 0.2664 were obtained. Substituting the obtained values of A $(-1,1)$ and B$(-1,1)$ into Equation (31), a remote sensing model for the friction velocity U_* was derived, as in Equation (33), that had the root-mean-square error (RMSE) of 0.02408 m/s.

$$U_* \approx -0.1928 \cdot \frac{Tb_{\text{upwelling}}(\theta_0, \varepsilon_{//})|_{H_0}}{Tb_{\text{downwelling}}(\vec{k_r})|_0} + 0.2664 \tag{33}$$

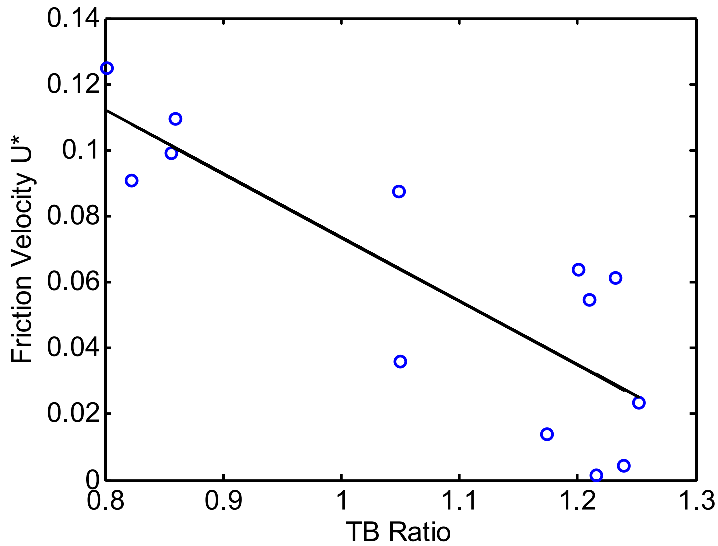

Figure 8. Friction velocity vs. TB ratio. The circles are the observed data on 21, 23 October 2018. The line in the figure was obtained by fitting the observed data using the least square method.

In this experiment, the fitting results in Figure 8 could only represent the characteristics of the LEATB under low sea state as all of the friction velocity data obtained were less than 0.14 m/s. The LEATB characteristics under high sea states should be fitted using measured data under high sea states. In addition, the applicability of the fitted coefficients A and B in this study might be limited to the study area where the wind speed data were measured by the AWS on the shore. In other words, the applicability for the ocean surface and the coastal area of Qingdao was highly restricted due to unreliable coefficients A and B.

5. Conclusions

In this paper, the characteristics of the X-band LEATBs and their relationships with the meteorological parameters of atmosphere and sea surface were analyzed using the measured data in the Qingdao sea area in China. The ground-based X-band atmospheric downwelling TB was sensitive more to the atmosphere at a lower elevation angle than that at a higher elevation. At low elevation angles, the diurnal TB variations varied day-by-day, i.e., 10 K on a day and 20 K on other days during the experiment period. The X-band horizontal polarization radiation TB in the elevation angle interval of $[-3°, 3°]$ showed the shape of the normal distribution, i.e., the maximum value in the middle and decreasing gradually to both sides. This study examined the composition mechanism of the LEATBs to understand this phenomenon. The influence of the atmospheric temperature and relative humidity on the atmospheric downwelling LEATBs at the X-band was also analyzed. On the contrary to the K and V band microwaves, neither atmospheric temperature nor atmospheric humidity played a leading role in the downwelling LEATBs in the X-band. The effects of the sea surface wind on the X-band horizontal polarization LEATBs under low sea state were analyzed. In the elevation angle interval of $[-3°, -1°]$, the measured LEATB under low sea state decreased as the wind speed increased, while, in $-5°$–$-10°$, the measured LEATB increased as the wind speed increased. The reason for this difference was analyzed theoretically. Further, this study showed that the LEATB difference was significantly influenced by the change in the OTHDC. Introducing intelligent algorithms, such as neural network, might improve the ability in the atmospheric ducts with regard to mining the information of the atmospheric duct contained in multi-elevation microwave radiation TBs and multiple bands, such as the X, Ku, K, V, and other bands. This study also proposed a semi-empirical model for remote sensing of the sea surface friction velocity under low sea state using the LEATB data at the elevation angles between $-1°$ and $1°$ and the wind speed data measured at 6 m altitude (U_6). The essential coefficients were obtained from the fitted line, and the semi-empirical model was successfully applied to calculate the sea surface friction velocity with the root mean square error (RMSE) of 0.02408 m/s.

Author Contributions: Conceptualization, Z.C., L.G. and S.K.; methodology, Z.C., L.G., S.K. and X.C.; software, Z.C.; validation, Z.C., L.G., S.K., X.C., Q.L., L.L. and Y.Z.; formal analysis, Z.C.; investigation, Z.C., L.G., S.K., X.C., Q.L., L.L. and Y.Z.; resources, Z.C., L.G., S.K., Q.L., L.L. and Y.Z.; data curation, Z.C.; writing—original draft preparation, Z.C.; writing—review and editing, Z.C. and L.G.; visualization, Z.C.; supervision, L.G.; project administration, L.G.; funding acquisition, Z.C. and L.G. All authors have read and agreed to the published version of the manuscript.

Funding: This study was supported by the National Natural Science Foundation of China (Grant No. 61627901, 61431010), the Foundation for Innovative Research Groups of the National Natural Science Foundation of China (Grant No.61621005).

Acknowledgments: We would like to thank Xiangming Guo and Xiaojing Hao for sharing the NPS model and WRF data and their constructive advice on how to use the model and data.

Conflicts of Interest: The authors declare no conflict of interest. The funders had no role in the design of the study; in the collection, analyses, or interpretation of data; in the writing of the manuscript, or in the decision to publish the results.

Appendix A

Relationship between Meteorological Parameters and Atmospheric Ducts

An atmospheric duct is an anomalous refraction structure driven by the anomalous distribution of meteorological parameters in an atmospheric boundary layer. When a duct occurs, the gradient of the atmospheric modified refractivity can be expressed as

$$dM/dh \leq 0 \quad \text{unit/km} \tag{A1}$$

where h is height, and M is the modified refractivity that can be expressed as a function of the atmospheric refractivity N as follows,

$$M = N + \frac{h}{a} \times 10^6 \tag{A2}$$

where a is Earth's radius in km. Therefore, the gradient of the atmospheric refractivity can be expressed as

$$dN/dh \leq -157\,N \quad \text{unit/km} \tag{A3}$$

N is a function of temperature T (Kelvin), the pressure of the water vapor e (millibar), and the pressure P (millibar), as in Equation (A4).

$$N = 77.6P/T - 5.6e/T + 3.75 \times 10^5 e/T^2 \tag{A4}$$

As the second term on the right of Equation (A4) is too small, it can be as

$$5.6e/T = (5.6T)e/T^2 \approx 0.016 \times 10^5 e/T^2 \tag{A5}$$

The temperature T in the numerator of Equation (A5) uses 288 K. Therefore, N can be expressed as

$$N = 77.6P/T + 3.73 \times 10^5 e/T^2 \tag{A6}$$

From Equations (A3) and (A6), the following can be deduced

$$\frac{dN}{dh} = \frac{\partial N}{\partial P} \cdot \frac{dP}{dh} + \frac{\partial N}{\partial T} \cdot \frac{dT}{dh} + \frac{\partial N}{\partial e} \cdot \frac{de}{dh} \quad \text{(A7)}$$

$$\frac{dT}{dh} \geq \frac{-157 - \left(\frac{\partial N}{\partial P} \cdot \frac{dP}{dh} + \frac{\partial N}{\partial e} \cdot \frac{de}{dh}\right)}{\frac{\partial N}{\partial T}} \quad \text{(A8)}$$

$$\text{and } \frac{de}{dh} \leq \frac{-157 - \left(\frac{\partial N}{\partial P} \cdot \frac{dP}{dh} + \frac{\partial N}{\partial T} \cdot \frac{dT}{dh}\right)}{\frac{\partial N}{\partial e}} \quad \text{(A9)}$$

As per the general conditions of $\partial N/\partial T < 0$, $\partial N/\partial e > 0$, $\partial N/\partial P > 0$, $dP/dh < 0$, $de/dh < 0$, the right side of Equation (A8) is greater than zero. Hence, the gradient of the temperature dT/dh is also greater than zero when an atmospheric duct occurs, which is called temperature inversion. Substituting the international civil aviation organization (ICAO) criterion for a standard atmosphere, i.e., $\partial N/\partial P = 0.27$ Nunit/mb, $\partial N/\partial T = -1.27$ Nunit/K, $\partial N/\partial e = 4.5$ Nunit/mb, $dP/dh = -120$ mb/km, and $de/dh = -3.7$ mb/km, into Equation (A8), Equation (A10) can be obtained.

$$\frac{dT}{dh} \geq 8.5\ ^{\circ}\text{C}/100\ \text{m} \quad \text{(A10)}$$

Equation (A10) represents that, under a standard atmosphere, the temperature inversion should be greater or equal to 8.5 °C/100 m to formulate an atmospheric duct.

Given that all of the other parameters are the same as above and $dT/dh = -6.5$ K/km, Equation (A9) can be simplified as follows,

$$\frac{de}{dh} \leq -2.95\ \text{mb}/100\ \text{m} \quad \text{(A11)}$$

Equation (A11) represents that, under a standard atmosphere, the requirement to formulate a duct is a humidity gradient less than or equal to −2.95 mb/100 m.

The atmospheric humidity and the wind speed are representative meteorological parameters that have the greatest impact on the atmospheric duct, followed by the atmospheric temperature, and the atmospheric pressure [21].

The NPS model incorporates the boundary layer similarity theory to simulate an evaporation duct using the atmospheric temperature, humidity, pressure, wind speed, and sea surface temperature as input data. An atmospheric duct profile over the sea surface can be obtained from the NPS model. As most of our observed data during the experiment were in the condition that the wind speed ranged from 0 m/s to 6 m/s, the conditions with wind speed higher than this range were calculated from the NPS model. In particular, this study investigated the influences of the wind speed and the atmospheric relative humidity on the evaporation ducts using outputs of the NPS model.

With other parameters fixed (10 m ASL, the atmospheric temperature of 18.8 °C, the atmospheric relative humidity of 50%, the pressure of 1023.5 hPa, sea surface temperature of 19.61 °C), except for the wind speed varying from 0.8 m/s to 10 m/s, the parameter values for height, strength, and trap angle of the evaporation ducts were calculated by the NPS model. The results showed that, under a stronger wind speed, the trap angle of the evaporation duct became larger, and the trapping ability of the evaporation duct was enhanced. These results are shown in Figure A1a,d.

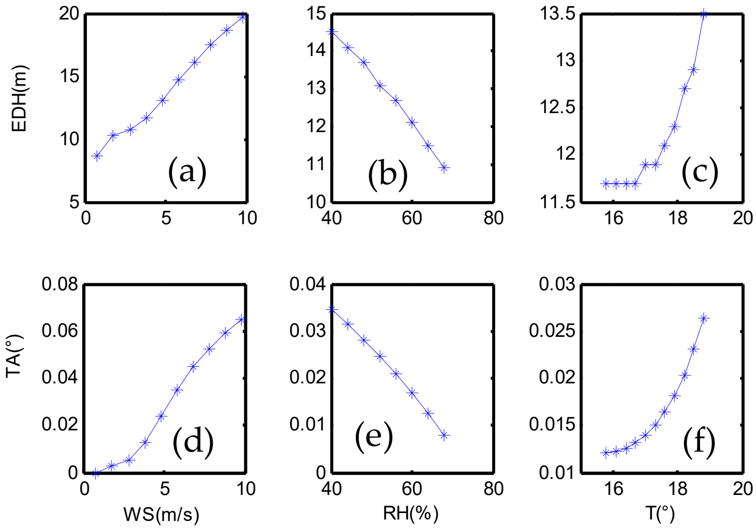

Figure A1. The effects of meteorological parameters on the evaporation ducts: (**a**) height of the evaporation duct (EDH) vs. the wind speed (WS), (**b**) the EDH vs. the relative humidity (RH), (**c**) the EDH vs. the temperature (T), (**d**) the trap angle (TA) vs. the wind speed, (**e**) the TA vs. the RH, and (**f**) the TA vs. the temperature.

With other parameters fixed (10 m ASL, the temperature of 18.8 °C, wind speed of 4 m/s, the pressure of 1023.5 hPa, sea surface temperature of 19.61 C), except for the atmospheric relative humidity varying from 40% to 70%, the evaporating duct height was calculated. The results showed that an increase in the relative humidity led to a decrease in the trapping angle of the evaporation duct and a weakened trapping effect of the evaporation duct, as shown in Figure A1b,e.

With other parameters fixed (10 m ASL, the relative humidity of 50%, wind speed of 4 m/s, the pressure of 1023.5 hPa, sea surface temperature of 19.61 °C), except for the atmospheric temperature varying from 15°C to 19°C, the evaporation duct height, strength, and trap angle were calculated. The results showed that as the atmospheric temperature increased, the trapping angles of the evaporation ducts increased, and the trapping effect of the evaporation ducts was enhanced, as shown in Figure A1c,f.

The results addressed above indicated that the temperature and the relative humidity had opposite influences on the evaporation duct, resulting in a tradeoff effect on the generation of the evaporation duct. For example, the duct increased as the temperature increased, while the duct decreased as the relative humidity increased.

References

1. Mack, S.; Padman, L.; Klinck, J. Extracting Tidal Variability of Sea. *Geophys. Res. Lett.* **2013**, *40*, 547–552. [CrossRef]
2. Sieron, S.B.; Zhang, F.; Kerry, A. Feasibility of Tropical Cyclone Intensity Estimation Using Satellite-Borne Radiometer Measurements: An Observing System Simulation Experiment. *Geophys. Res. Lett.* **2013**, *40*, 1–5. [CrossRef]
3. Meissner, T.; Wentz, F.J. The Emissivity of the Ocean Surface Between 6 and 90 GHz Over a Large Range of Wind Speeds and Earth Incidence Angles. *IEEE Trans. Geosci. Remote Sens.* **2012**, *50*, 3004–3026. [CrossRef]
4. Brown, S.T.; Ruf, C.S.; Lyzenga, D.R. An Emissivity-Based Wind Vector Retrieval Algorithm for the WindSat Polarimetric Radiometer. *IEEE Trans. Geosci. Remote Sens.* **2006**, *44*, 611–621. [CrossRef]
5. Ebuchi, N. Evaluation of Marine Surface Wind Speed Observations from AMSR2 on GCOM-W Satellite. *IEEE J. Sel. Top. Appl. Earth Obs. Remote Sens.* **2017**, *10*, 3955–3962. [CrossRef]
6. Carolina, B.T.; Yazan, H.; Jacob, M.M.; Jones, W.L. An Algorithm for Sea Surface Wind Speed from SAC-D/Aquarius Microwave Radiometer. *IEEE J. Sel. Top. Appl. Earth Obs. Remote Sens.* **2015**, *12*, 5485–5502.

7. Zhang, L.; Yin, X.B.; Shi, H.Q.; Wang, Z.Z. Hurricane Wind Speed Estimation Using WindSat 6 and 10 GHz Brightness Temperatures. *Remote Sens.* **2016**, *8*, 721. [CrossRef]
8. Zhang, L.; Yin, X.B.; Shi, H.Q.; Wang, Z.Z.; Xu, Q. Estimation of wind speeds inside super Typhoon Nepartak from AMSR2 low frequency brightness temperatures. *Remote Sens.* **2019**, *13*, 124–131. [CrossRef]
9. Yueh, S.H.; Fore, A.G.; Tang, W.Q.; Hayashi, A.; Stiles, B.; Reul, N.; Weng, Y.H.; Zhang, F.Q. SMAP L-Band Passive Microwave Observations of Ocean Surface Wind During Severe Storms. *IEEE Trans. Geosci. Remote Sens.* **2016**, *54*, 7339–7350. [CrossRef]
10. Sun, Z.Y.; Zhang, B.; Zhang, J.A.; William, P. Examination of Surface Wind Asymmetry in Tropical Cyclones over the Northwest Pacific Ocean Using SMAP Observations. *Remote Sens.* **2019**, *11*, 2604. [CrossRef]
11. Chen, Z.Z.; Chen, X.; Zhao, C.; Li, J.; Huang, W.M.; Gill, E.W. Observation and Intercomparison of Wave Motion and Wave Measurement Using Shore-Based Coherent Microwave Radar. *IEEE Trans. Geosci. Remote Sens.* **2019**, *57*, 7594–7605. [CrossRef]
12. Xie, J.H.; Yao, G.W.; Sun, M.L.; Ji, Z.Y. Measuring Ocean Surface Wind Field Using Shipborne High-Frequency Surface Wave Radar. *IEEE Trans. Geosci. Remote Sens.* **2018**, *56*, 3383–3397. [CrossRef]
13. Dankert, H.; Horstmann, J.; Rosenthal, W. Wind- and Wave-Field Measurements Using Marine X-Band Radar-Image Sequences. *IEEE J. Ocean. Eng.* **2005**, *30*, 534–542. [CrossRef]
14. Zhang, Y.; Zhang, S.W.; He, J.Y. Design and Development of a Ground-Based Microwave Radiometer System. In Proceedings of the Progress in Electromagnetics Research Symposium (PIERS ONLINE). 2010, Volume 6, pp. 66–70. Available online: http://www.piers.org/piersonline/pdf/Vol6No1Page66to70.pdf?origin=publication_detail (accessed on 2 April 2020).
15. Renju, R.; Raju, C.S.; Mishra, M.K.; Mathew, N.; Rajeev, K.; Moorthy, K.K. Atmospheric Boundary Layer Characterization Using Multiyear Ground-Based Microwave Radiometric Observations Over a Tropical Coastal Station. *IEEE Trans. Geosci. Remote Sens.* **2017**, *55*, 6877–6882. [CrossRef]
16. Cadeddu, M.P.; Payne, V.H.; Clough, S.A.; Cady-Pereira, K.; Liljegren, J.C. Effect of the Oxygen Line-Parameter Modeling on Temperature and Humidity Retrievals from Ground-Based Microwave Radiometers. *IEEE Trans. Geosci. Remote Sens.* **2007**, *45*, 2216–2223. [CrossRef]
17. Liu, D.; Lv, C.; Liu, K.; Xie, Y.; Miao, J. Retrieval Analysis of Atmospheric Water Vapor for K-band Ground-Based Hyperspectral Microwave Radiometer. *IEEE Geosci. Remote Sens. Lett.* **2014**, *11*, 1835–1839.
18. Padmanabhan, S.; Reising, S.C.; Vivekanandan, J.; Iturbide-Sanchez, F. Retrieval of Atmospheric Water Vapor Density with Fine Spatial Resolution Using Three-Dimensional Tomographic Inversion of Microwave Brightness Temperatures Measured by a Network of Scanning Compact Radiometers. *IEEE Trans. Geosci. Remote Sens.* **2009**, *47*, 3708–3721. [CrossRef]
19. Steinke, S.; Löhnert, U.; Crewell, S.; Liu, S. Water Vapor Tomography with Two Microwave Radiometers. *IEEE Geosci. Remote Sens. Lett.* **2014**, *11*, 419–423. [CrossRef]
20. Schween, J.H.; Crewell, S.; Löhnert, U. Horizontal Humidity Gradient from One Single Scanning Microwave Radiometer. *IEEE Geosci. Remote Sens. Lett.* **2011**, *8*, 336–340. [CrossRef]
21. Sumati, R. Statistical Retrieval of the Water Vapor Profiles Using Zenith-Pointing and Off-Axis 22GHz Radiometer Measurements. Ph.D. Thesis, The Pennsylvania State University, State College, 201 Old Main, University Park, PA, USA, 1998.
22. Louf, V.; Pujol, O.; Sauvageot, H. The Seasonal and Diurnal Cycles of Refractivity and Anomalous Propagation in the Sahelian Area from Microwave Radiometric Profiling. *J. Atmos. Ocean. Technol.* **2016**, *33*, 2095–2112. [CrossRef]
23. D'Orazio, A.; Sario, M.D.; Gramegna, T.; Petruzzelli, V.; Prudenzano, F. Optimisation of Tipping Curve Calibration of Microwave Radiometer. *Electron. Lett.* **2003**, *39*, 905–906. [CrossRef]
24. Crewell, S.; Czekala, H.; Lohnert, U.; Simmer, C. Microwave Radiometer for Cloud Cartography: A 22-Channel Ground-Based Microwave Radiometer for Atmospheric Research. *Radio Sci.* **2001**, *36*, 621–638. [CrossRef]
25. Maschwitz, G.; Lohnert, U.; Crewell, S.; Rose, T.; Turner, D. Investigation of Ground-Based Microwave Radiometer Calibration Techniques at 530 hPa. *Atm. Meas. Tech.* **2013**, *6*, 2641–2658. [CrossRef]
26. Ulaby, F.T.; Moore, R.K.; Fung, A.K. *Microwave Remote Sensing: Active and Passive. Volume 2: Radar Remote Sensing and Surface Scattering and Emission Theory*; Addison-Wesley, Advanced Book Program: Reading, MA, USA, 1982; p. 609.
27. Wentz, F.J. A model Function for Ocean Microwave Brightness Temperatures. *J. Geophys. Res.* **1983**, *88*, 892–908. [CrossRef]

28. Peake, W. Interaction of Electromagnetic Waves with Some Natural Surfaces. *IRE Trans. Antennas Propag.* **1959**, *7*, 324–329. [CrossRef]
29. Yin, X.; Boutin, J.; Dinnat, E.; Song, Q.; Martin, A. Roughness and Foam Signature on SMOS-MIRAS Brightness Temperatures: A Semi-Theoretical Approach. *Remote Sens. Environ.* **2016**, *180*, 221–233. [CrossRef]
30. Cheng, J.; Cheng, X.; Meng, X.; Zhou, G. A Monte Carlo Emissivity Model for Wind-Roughened Sea Surface. *Sensors* **2019**, *19*, 2166. [CrossRef]
31. Wentz, F.J. A Two-Scale Scattering Model for Foam-Free Sea Microwave Brightness Temperatures. *J. Geophys. Res.* **1975**, *80*, 3441–3446. [CrossRef]
32. Garrison, J.L.; Komjathy, A.; Zavorotny, V.U.; Katzberg, S.J. Wind Speed Measurement Using Forward Scattered GPS Signals. *IEEE Trans. Geosci. Remote Sens.* **2002**, *40*, 50–65. [CrossRef]
33. Wang, Y.; Zhang, Y.; Chen, H.; Guo, L. Effects of Atmospheric Stability and Wind Fetch on Microwave Sea Echoes. *IEEE Trans. Geosci. Remote Sens.* **2014**, *52*, 929–935. [CrossRef]
34. Bourlier, C. Propagation and scattering in ducting maritime environments from an accelerated boundary integral equation. *IEEE Trans. Antennas Propag.* **2016**, *64*, 4794–4803. [CrossRef]
35. Zhao, X.F.; Yang, P.L. A simple two-dimensional ray-tracing visual tool in the complex tropospheric environment. *Atmosphere* **2017**, *8*, 35. [CrossRef]
36. Colussi, L.C.; Schiphorst, R.; Teinsma, H.W.M.; Witvliet, B.A.; Fleurke, S.R.; Bentum, M.J.; van Maanen, E.; Griffioen, J. Multiyear trans-horizon radio propagation measurements at 3.5 GHz. *IEEE Trans. Antennas Propag.* **2018**, *66*, 884–896. [CrossRef]
37. Paulus, R.A. Evaporation Duct Effects on Sea Clutter. *IEEE Trans. Antennas Propag.* **1990**, *38*, 1765–1771. [CrossRef]
38. Frederickson, P.A.; Davidson, K.L.; Goroch, A.K. Operational bulk evaporation duct model for MORIAH, Naval Postgraduate School Report, Version 1. *2*. 2000.
39. Babin, S.M.; Dockery, G.D. LKB-based evaporation duct model comparison with buoy data. *J. Appl. Meteorol.* **2002**, *41*, 434–446. [CrossRef]
40. Pons, J.; Reising, S.C.; Padmanabhan, S.; Camps, A.; Duffo, N. Passive Polarimetric Remote Sensing of the Ocean Surface During the Rough Evaporation Duct Experiment (RED 2001). In Proceedings of the IGARSS 2003, Toulouse, France, 21–25 July 2003.
41. Sethuraman, S.; Raynor, G.S. Surface Drag Coefficient Dependence on the Aerodynamic Roughness of the Sea. *J. Geophys. Res.* **1975**, *80*, 4983–4988. [CrossRef]